# Mesoscale FDDA Experiments with ACARS Data

**Chia-bo Chang**
**Geosciences, Texas Tech University, Lubbock, TX**

**Robert Dumais**
**U.S. Army Research Laboratory,**
**White Sands Missile Range, NM 88002**

## 1. Introduction

The focus of this paper is on mesoscale four-dimensional data assimilation (FDDA). Because of its small spatial size, mesoscale weather is strongly influenced by fast-changing local conditions such as cloud cover, friction, and surface heating.  To incorporate these fast-changing events so as to maximize the model performance, state-of-the-art mesoscale numerical weather prediction (NWP) often makes use of FDDA of high-frequency observations to update the model state during the time integration (Daley 1991). The NOAA ACARS (Aircraft Communications Addressing and Reporting System) observations taken by commercial aircraft at about every ten minutes crisscrossing the nation (Mamrosh 1998) offer valuable data for mesoscale FDDA. Other researchers such as at NCAR's Research Applications Laboratory (Sheu et al, 2002; Liu et al, 2004) have provided some previous examination of the impact and quality of ACARS in mesoscale FDDA. A better understanding of how to take advantage of these high resolution data sets can significantly advance our expertise in mesoscale NWP.

A method known as observational nudging (Newtonian relaxation) is employed in the FDDA experiments. This empirical approach is based on the work by Hoke and Anthes (1976). There are other more sophisticated FDDA methods involving the Kalman filter or three-dimensional variational (3DVAR) procedures (Kalnay 2003), but these advanced treatments are much more computationally intensive and require background information generally not available in a fast-response scenario. We believe that the simple Newtonian relaxation technique represents a good balance between complexity, timeliness, and accuracy, which is an important guiding principle for short-term prediction and nowcasting.

The results of a real-data case study including several 36-h model simulations using the 5th generation Mesoscale Modeling System (MM5) (Grell et al, 1994)  are presented. We are particularly interested in the impact of mesoscale FDDA on boundary layer (BL) and precipitation forecasting. The sensitivity of model forecasts to changes in (1) the nudging parameters and (2) the input data density are also examined.

## 2. ACARS

These data are routed by several cooperating airlines to the NOAA GSD (Global Systems Division) for quality control. General information about ACARS included how to access the data sets can be found on the website acweb.fsl.noaa.gov. ACARS wind and temperature data are collected by many commercial aircraft during both en route and ascent/descent modes of their

flights at a very high frequency. At flight altitudes of about 23,000 ft, data are generally taken every 5-6 minutes. Near the airports the data spacing is decreased by some airlines. Below 18,000 ft, a vertical resolution of 1000 to 2000 ft is quite common. More than 150 aircraft provide data with a vertical resolution of about 300 ft for the first minute after take-off. ACARS can certainly provide useful up-to-date weather information for short-range forecasts.

The quality of ACARS data had been examined by many researchers, e.g., <u>Mamrosh (1998)</u>, <u>Schwartz and Benjamin (1995)</u>, and <u>Lord, et. al. (1984)</u>. Estimated wind vector accuracy was about 1.8 m/s and estimated temperature accuracy was about $0.5^{o}$C. When ACARS was compared to radiosondes, root mean square (RMS) deviations were 7.4 degrees in direction and 5.3 m/s in speed. In comparing ACARS ascent/descent winds and temperatures with radiosondes, it was found that temperature differences were less than $2^{o}$C on 94 percent of all occasions, and less than $1^{o}$C greater than 68 percent of the time. Wind speed RMS deviations were 4.1 m/s, while direction RMS differences were 35 degrees (mostly due to light and variable wind situations).

**3. MM5/FDDA Experiments**

The MM5 BL scheme over land comprises two basic regimes: nocturnal and free convection.  The following BL-related physical options are selected for the simulation experiments:
• Grell moist-convection parameterization
• Atmospheric radiation with the effects of clouds (Dudhia et al. 1998).
• MRF (Hong and Pan 1996) planetary boundary layer
• Surface heat and moisture fluxes from the ground
• Surface energy budget to calculate the ground temperature
• Multi-layer soil thermal diffusion

We experimented with various nesting options in MM5, trying one-, two-, and three-nest configurations in conjunction with horizontal grid sizes ranging from 3 km to 20 km. The model appeared to be quite reliable and robust, and close examination of model output did not reveal any indication of computational instability during the model integrations.

Some basic features of the single-grid MM5 modeling configuration adopted in this study are presented in Table 1, while Fig. 1 shows the model domain and terrain. The severe weather event of 8-9 May 2005 which occurred in Central Texas was selected for the case study experiments. The model initial and lateral boundary conditions were derived from the NWS/NCEP ETA model (Black, 1994), which had 50 vertical levels and a horizontal grid spacing of 22 km. All model integrations were performed on a SGI Octane 2 workstation.

| Horiz  dimens & spacing | Vert  σ levels | Length | Form | Start time UTC/dy/mn |
|---|---|---|---|---|
| (67x67)/20 km | 24 | 36 h | Non-hydrostatic | 00/08/05 |

**Table 1.  Key MM5 Case Study Parameters**

First we carried out a 36-h simulation of the severe weather environment, which involved  a dryline perturbation in West Texas and intense convection in Central Texas. This simulation did not include ACARS data and is used as the control run (CNTR) to provide a benchmark for

2

measuring the impact of FDDA. In the subsequent FDDA runs, more than 90 ACARS profiles collected across several Mountain and South Central states (Fig. 2) were used for observational nudging. In the lower and middle layers, clusters of ACARS reports aligned approximately in the north-south direction were found in central Texas and Oklahoma. The data coverage was spread more uniformly in the upper layers. Each data point recorded during a flight (at a given time, latitude, longitude, and altitude) was treated as one single independent observation. The locations of individual observations in terms of the model grid system had to be determined first, and they were organized in order of increasing time as required by the MM5 nudging program. Explanations for the input data structure as well as the details of the observational nudging scheme can be found in the MM5 tutorial notes under the section of Data Used in FDDA (Grell et al. 1994).

The ACARS observations obtained for the case study initially consisted of 1928 data points of wind and temperature fields. The number dropped to 1213 after averaging observations within the same proximity, meaning that they were reported in the same time slot and at the same vertical level while within 10 km (half the grid size of the individual model grid points). Many more observations were inserted into the model upper layers than the middle and lower layers. The first experiment (E1) was a 36-h run with 12-h observational nudging between 12 h and 24 h of model integration based on the averaged data set.

The nudging parameters selected in E1 were as follows:
• Nudging factors (N) for wind and temperature are $4 \times 10^{-4}$ $s^{-1}$.
• Horizontal radius of influence (R) is 100 km from the observation site.
• Vertical radius of influence ($\Delta\sigma$) is 0.001 centered at the level of $\sigma = 0.995$.
• Time window ($\Delta t$) is 30 min centered at the observation time.

An additional three experiments were conducted to test the model's response to changes in R, N, and data density.
- E2 similar to E1 but R = 50 km.
- E3 similar to E1 but N = $2 \times 10^{-4}$ $s^{-1}$.
- E4 similar to E1 but with all 1928 data points without the averaging procedure.

### 3.1 CNTR vs. E1

Figure 3 shows the initial state at the surface and 700 hPa at 00 UTC May 8 2005. A north-south oriented dryline is evident in the middle of the model domain. The major features at the surface are southerly flow to the east of the dryline and southwesterly flow to the west, creating a confluence of air near the dryline. Notable changes in the wind directions from southerly at the surface to westerly at 700 hPa (veering profile) occur in South Texas. The 700 hPa confluent zone is located in Central Texas and Oklahoma well to the east of the dryline. The average wind speed at 700 hPa is on the order of 10 m/s, while at 300 mb (not shown) the flow is predominantly southwesterly with a relatively narrow zone of winds in excess of 30 m/s stretching from Mexico to the northern boundary of the domain. This stronger zone of 300 mb flow generally occurs over the area of the dryline. Fig. 4 shows the observed surface vector winds and surface $T_d$ at 12 UTC 9 May 2005. Throughout the 36-h period, across Central Texas the southerly surface flow persists and continues to advect moisture inland from the Gulf of

3

Mexico. The $T_d$ gradients along the dry line in West Texas tighten, although they do weaken considerably in the Panhandle. The result is a double boundary surface $T_d$ structure enclosing a diffluence area of relatively weak surface winds. Again, there is confluence associated with the dryline. No upper-air jet features appear in the model domain during this time.

Figure 5 shows 24-h and 36-h simulated surface winds and $T_d$ from the CNTR run. Throughout the first 24 h, a significant weakening of surface circulation occurred in the western half of the domain. The MM5 predicted a large increase in the $T_d$ gradients in West Texas and a northeastward intrusion of dry air and resulting dryline bulging into regions of western Kansas and the Oklahoma Panhandle. At 36 h, the middle section of the dryline retreated slightly westward and aligned along the Texas-New Mexico border. The observed double-boundary structure (Fig. 4) and tight $T_d$ gradients were well predicted but the model dryline in the Texas Panhandle area was located too far to the west. This was likely caused by the MM5 over-prediction of southerly flow which served to advect the moister air mass further northwestward into the Texas Panhandle. Clearly, surface convergence played a key role in the intensification and maintenance of the sharp $T_d$ gradients. The model convective precipitation rates revealed that there was no organized activity before 18 h, and that convection in Oklahoma and West Texas along the eastern edge of the dryline took place from 18 h to 30 h. Fig. 6 depicts the model convective precipitation rates at 24 and 36 h, with the activity reaching its peak intensity around 24 h and tailing off over the next 12 h. Note that no convection is present near the dryline at 36 h. Also, the major activities are found quite far away from the dryline in Central and East Texas, where severe weather was reported.

Figure 7 shows the 36-h simulated surface winds and $T_d$ in E1. The large differences in the wind and $T_d$ fields between CNTR and E1 occurred in West Texas and eastern New Mexico, e.g., the location and orientation of the dryline and confluence zone. The model convective rainfall rates in CNTR and E1 were rather similar before 24 h, but they differed from each other quite a bit in the last 12 h. E1 produced bands of heavy convection (not shown) further to the west of the area of major activities in CNTR. Figs 8 and 9 show the 36-h simulated accumulated precipitation in CNTR and E1, respectively. Some direct influences of the MM5 eastern grid boundary on the model accumulated precipitation fields are noted, although the general patterns compare quite well with those observed and shown in Fig. 10. In CNTR, an area of over 10 cm of rainfall is shown in North Texas, while in E1 a similar maximum is centered further to the south. The basic features, in particular the location, of heavy rainfall (> 2.5 cm) in the middle of Texas in E1 appear to be in better agreement with the observations than in CNTR.

Although the nudging of ACARS data ends at 24 h, its impact on the MM5 simulations persists in the next 12 h. Fig. 11 shows the difference (CNTR-E1) maps of surface vector winds ($\Delta V$), surface temperatures ($\Delta T$), and specific humidity ($\Delta q$) at 24 and 36 h. Note that no q data were used in nudging. Clearly, $\Delta V$ is compounded by latent heating. The locations of the $\Delta V$, $\Delta T$, and $\Delta q$ centers are well correlated with each other at 24 h but not as well at 36 h. At 24 h, over 15 m/s $\Delta V$ are found in many locations, and $\Delta T$ and $\Delta q$ also show several maximum and minimum centers with values as large as $6^o$C and 7 gm/kg respectively scattering across Texas and Oklahoma. Twelve hours later there still exist areas of large $\Delta V$. However, we see clear fading of $\Delta T$ in the 12-h period. At 36 h, the most pronounced $\Delta q$ in the vicinities of the Kansas-Oklahoma

4

as well as Texas-New Mexico state lines is due to the discrepancy in the predicted location and orientation of the dryline.

Figure 12 shows (CNTR-E1) and (E1-CNTR) in the 36-h accumulated precipitation ($\Delta P$). The CNTR run produced a broad area of much higher rainfall in North Texas with the largest $\Delta P$ over 5 inches and several smaller areas of positive $\Delta P$ further south. E1 produced much heavier rainfall in the central section of Texas. The observed patterns in Fig. 10 appear to support the high positive (E1-CNTR) $\Delta P$ in Texas as well as the area of positive $\Delta P$ at the Oklahoma-Texas border. The bulk of $\Delta P$ was caused by large rainfall differences between the two runs in the last 12 h, suggesting significant influences of ACARS data on the model precipitation processes hours after ending FDDA.

Figure 13 summarizes the time sequences of means and standard deviations (SDs) of (CNTR-E1) differences in the surface winds ($\Delta u$ and $\Delta v$) and $\Delta T$. Some oscillations are noted in the mean values between 12 and 36 h. The SDs of $\Delta u$, $\Delta v$, and $\Delta T$ increase rapidly as FDDA starts at 12 h, but the SD of $\Delta q$ (not shown) increases gradually before 20 h because the ACARS profiles do not include q. The SDs of $\Delta u$ and $\Delta v$ reach their highest values around 30 h a few hours after the termination of FDDA, while SD of $\Delta T$ reaches its maximum at 24 h. At the end of simulations, all SDs remain quite high and close to those at 24 h. Fig. 14 shows the similar means and SDs at a middle level. Again, the SDs remain high at the end of simulation. For both levels, the amplitudes of oscillations are not particularly large and show very little temporal variations. There are no coherent relationships in the frequency and phase between the individual variables as well as between the two levels. FDDA in this case resulted in a warmer and dryer model surface, but a cooler and moister model mid-troposphere.

Figure 15 shows the means and SDs of forecast errors (observations-model) at the model levels for CNTR. The mean curves suggest that the MM5 CNTR run over-predicted u (except near the surface), but generally under-predicted v. The SD curves suggest that for u and v MM5 performed better below Level 6.  The MM5 CNTR run performed best for T in the upper layers above Level 14, and worst for T near the surface (where the model was too cold). The 36-h root mean square (RMS) errors of u, v, and T have about the same size as those of 24-h values for typical regional model forecasts summarized by Anthes (1983). There are very minor differences in the means and SDs of forecast error between CNTR and E1. FDDA clearly alters the model wind, T, and precipitation forecasting, but it is difficult to identify such impact in terms of the more common forecast error statistical measures.

### 3.2 E2, E3, and E4

These three experiments are designed to examine how MM5 FDDA responds to changes in the magnitude of nudging parameters and radii of influence. Inter-comparisons based on the means and SDs of forecast errors show minimal differences between CNTR and the individual runs. However, some interesting variations are noted in the model precipitation forecasts. The basic structure and magnitudes of (CNTR-E4) and (E4-CNTR) in the simulated 36-h accumulated rainfall strongly resemble those of (CNTR-E1) and (E1-CNTR) depicted in Fig. 12a and b, respectively. The similar departures of E2 and E3 from CNTR are summarized in Fig. 16. The general patterns of (CNTR-E1) bear some resemblance to those of (CNTR-E2) or (CNTR-E3).

5

However, (E2-CNTR) and (E3-CNTR) have a less organized configuration with many isolated centers and differ considerably from (E1-CNTR). As for rainfall prediction, the MM5 model appears to be less affected by the removal of proximate data in E4 than the reduction of the horizontal radius of influence in E2 or the nudging factor in E3. Also, all experiments except CNTR produced an area of heavy rainfall adjacent to the Texas-Oklahoma border as observed.

## 4. Summary

The study is designed to test the underlying hypothesis that high frequency mesoscale FDDA using the observational nudging method can significantly improve mesoscale NWP. The work was carried out based on MM5 real-data simulation experiments in conjunction with ACARS profile data. The severe weather event of 8-9 May 2005 occurring over Central Texas was selected for the experiments, which included a control run and several FDDA runs. The area means of model difference fields between the control run and individual FDDA runs showed some temporal oscillations with relatively small amplitudes suggesting that the model was only undergoing mild adjustments to the insertion of ACARS data. The corresponding standard deviations revealed lasting impact of the profile data on the MM5 forecasts throughout the entire model atmosphere 12 h after the termination of FDDA. The data distribution was not very uniform in the middle and lower layers. Some large changes (control minus FDDA) in the surface flow and temperatures were found far away from the areas where the data were concentrated. While ACARS caused substantial variations in precipitation and surface flow forecasting, the results suggest it was difficult to identify such impact, whether positive or negative, in terms of forecast statistics from a single case study.

The model responses to data assimilation are likely to vary with weather scenarios and the size of data sets. Nevertheless, the experiments have shown that ACARS data has high potential to advance our expertise in short-term mesoscale modeling and supporting the need to rapidly and accurately adjust high-resolution meteorological model forecasts to near real-time observations. More case studies of diverse events (e.g., oscillation drylines, rainstorms, wind/dust storms) are desired, particularly those which occur in the vicinity of the West Texas Mesonet domain. This will enable us to carry out comprehensive model validation with the Mesonet tower T, wind, and rainfall observations. It will hopefully allow us to reveal the most likely areas for great improvement using the composite forecast statistics derived from a large number of diverse mesoscale weather events.

**REFERENCES**
.
Anthes, R. A., 1983: Regional models of the atmosphere in middle latitudes. *Mon. Wea. Rev.*, **111**, 1306-1335.

Black, T.L., 1994. The New NMC Mesoscale Eta Model: Description and Forecast Examples. *Wea. Forecasting* 9(2): 265- 278.

Daley, R., 1991: *Atmospheric Data Analysis*. Cambridge University Press. Cambridge.

Dudhia, J., Gill, D., Guo, Y.-R., Hansen, D., and Manning, K., 1998. PSU/NCAR Mesoscale Modeling System Tutorial Class Notes and User's Guide: MM5 Modeling System Version 2. National Center for Atmospheric Research, Boulder, CO.

Grell, A. G., J. Dudhia, and D. R. Stauffer, 1994: A description of the fifth generation Penn State/NCAR mesoscale model (MM5). Mesoscale and Microscale Meteorology Division, NCAR, Boulder, CO.  122 pp.

Hoke, J. E. and R. A. Anthes, 1976: The initialization of numerical models by a dynamic initialization technique. *Mon. Wea. Rev*., 104, 1551-1556.

Hong, S.-Y., and H.-L. Pan, 1996: Non-local boundary layer vertical diffusion in a medium–range forecast model. *Mon. We. Rev.*, 124, 2322-2339.

Kalnay, E., 2003: *Atmospheric Modeling, Data Assimilation and Predictability*. Cambridge University Press.

Liu, Y., F. Vandenberghe, S. Low-Nam, T. Warner and S. Swerdlin, 2004: Observation-quality estimation and its application in the NCAR/ATEC real-time FDDA and forecast (RTFDDA) system. 16th Conference on Numerical Weather Prediction , Seattle, Washington. January, 2004. PAPER J1.7.

Lord, R. J., W. P. Menzel, and L. E. Pecht, 1984: ACARS Wind Measurements: An Intercomparison with Radiosonde, Cloud Motion, and VAS Thermally-Derived Winds. *J. Oceanic and Atmos. Tech*., 1, 131-137.

Mamrosh, R. D. 1998: The use of high-frequency ACARS soundings in forecasting convective storms. Weather and Forecasting Conference, AMS, January 12-16, 1997, Phoenix, AZ

Schwartz, B. E., and S. C. Benjamin, 1995: A Comparison of Temperature and Wind Measurements from ACARS-Equipped Aircraft and Rawinsondes. *Wea. Forecasting,* **10**, 528-544.

Sheu, R-S., Y. Liu, S. Low-Nam and L. Carson, 2002: The impact of Assimilating ACARS data on the performance of a real-time FDDA weather analysis and forecasting system. *Symposium on Observations, Data assimilation and Probablisitic Prediction*, 13-18 January 2002, Orlando, FL.
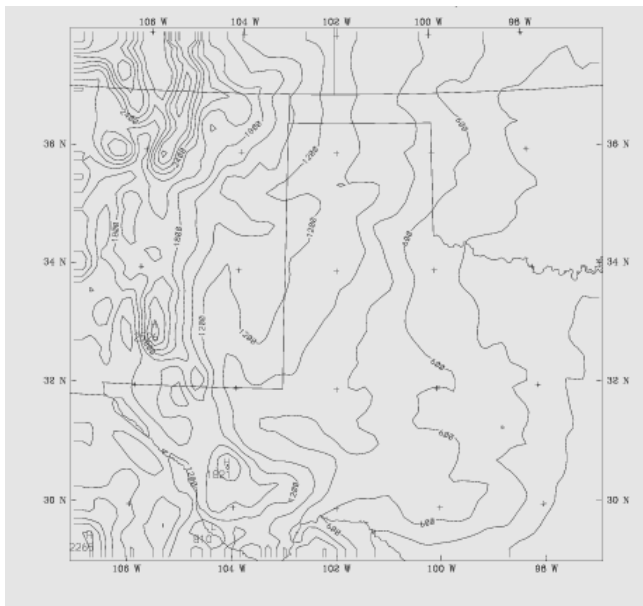
Fig. 1 MM5 model domain and terrain. The terrain contour interval is 200 m.



(a)



(b)



8
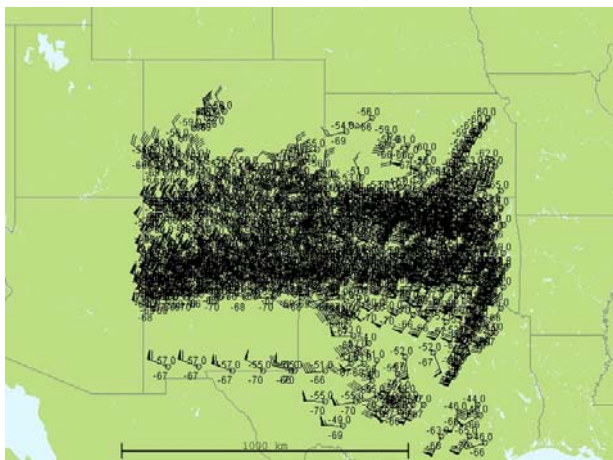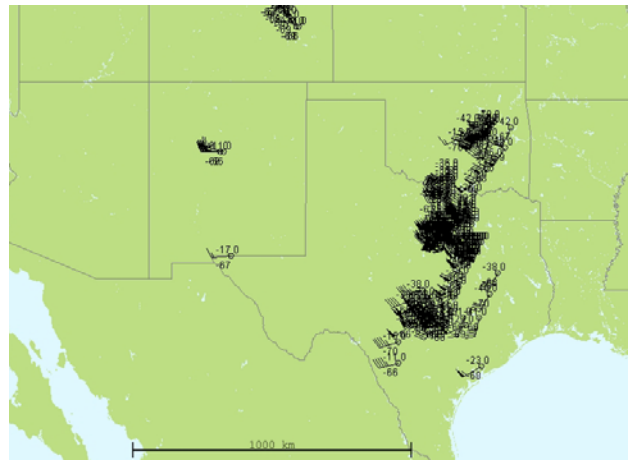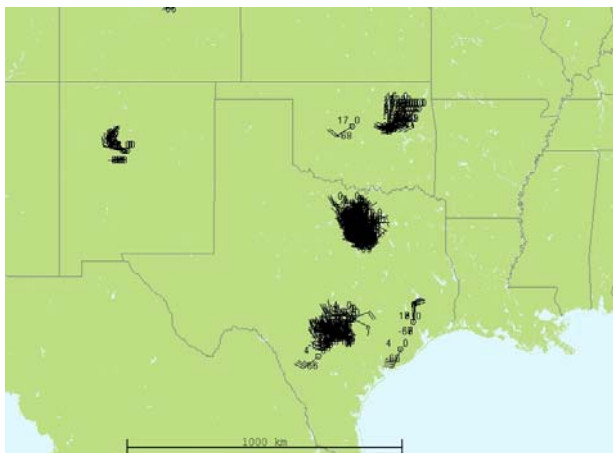
Fig.2 ACARS observation sites, 12 UTC 8 to 00 UTC 9 May 2005. (a) upper layers centered at 300 hPa, (b) middle layers centered at 500 hPa, and (c) lower layers centered at 700 hPa.



(a)



(b)
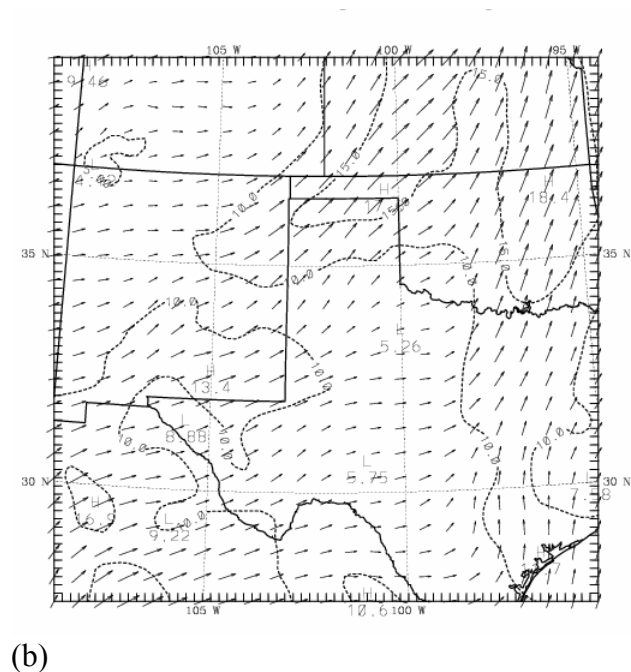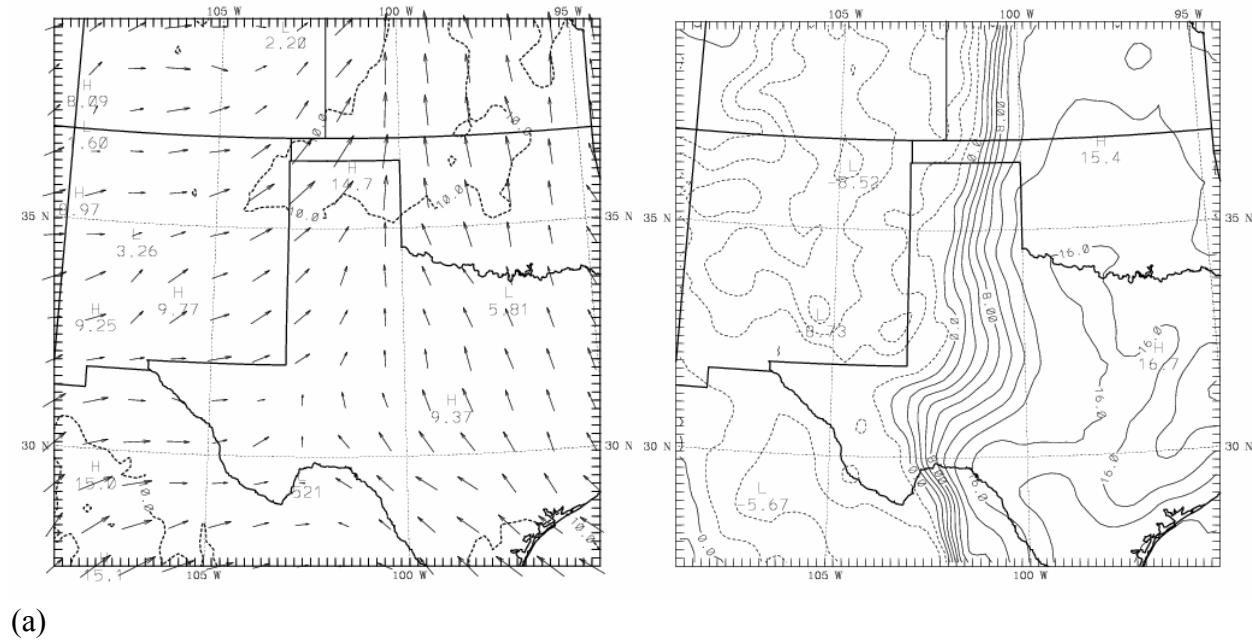
Fig. 3 MM5 initial state: (a) surface vector winds (m/s) and $T_d$ ($^{o}$C) and (b) 700 hPa vector winds.
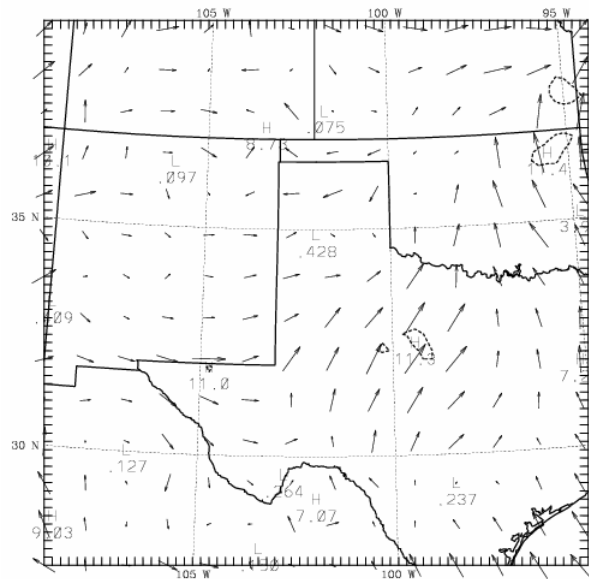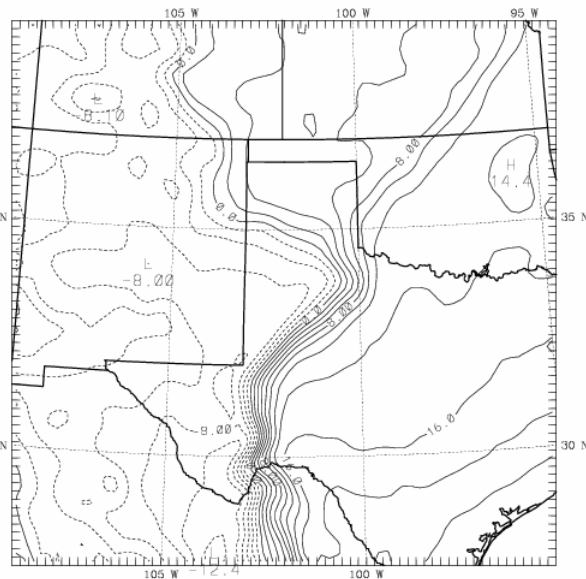
(a)                                                    (b)

Fig. 4 Observed surface conditions at 12 UTC 9 May. (a) vector winds (m/s) and (b) $T_d$ ($^o$C)
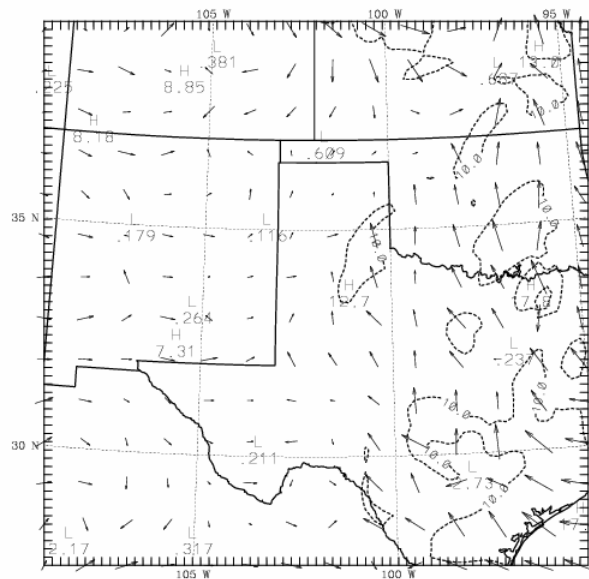
(a)
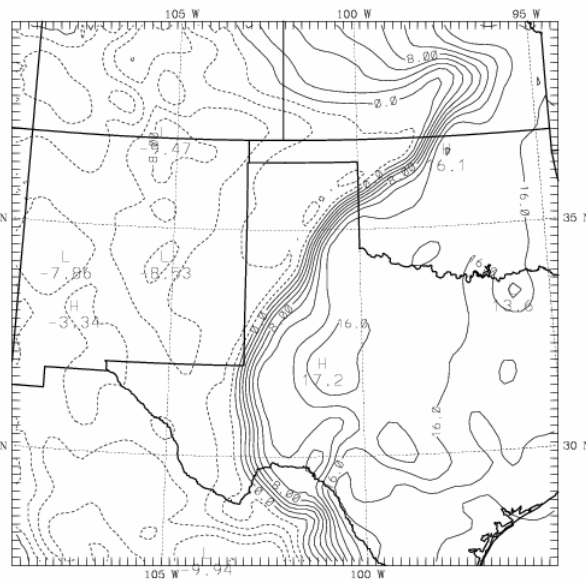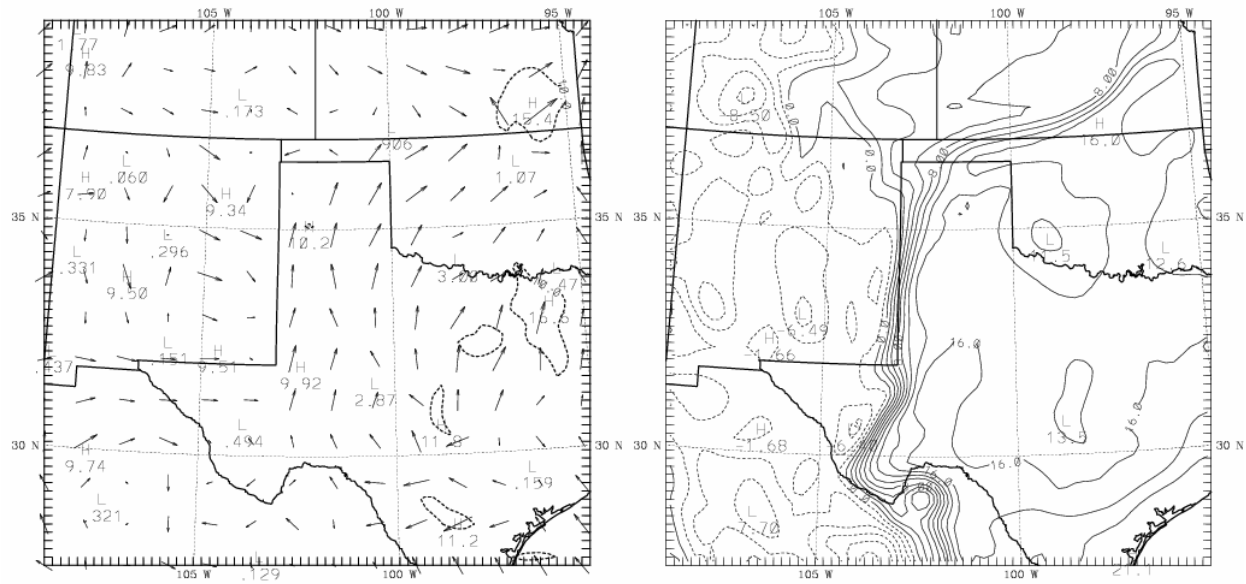
(b)

Fig. 5 Simulated surface vector winds (m/s) and $T_d.(^oC)$ at (a) 24 h and (b) 36 h for CNTR
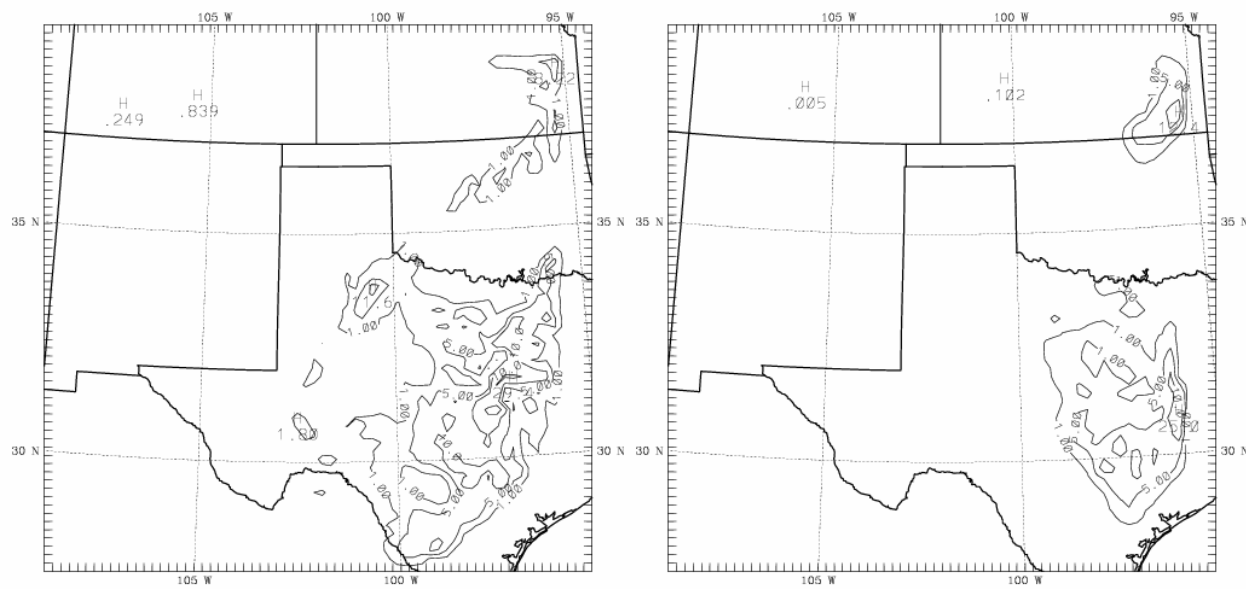
(a)                                                                    (b)

Fig. 6 Simulated convective precipitation rate (mm) at (a) 24 h and (b) 36 h for CNTR

11
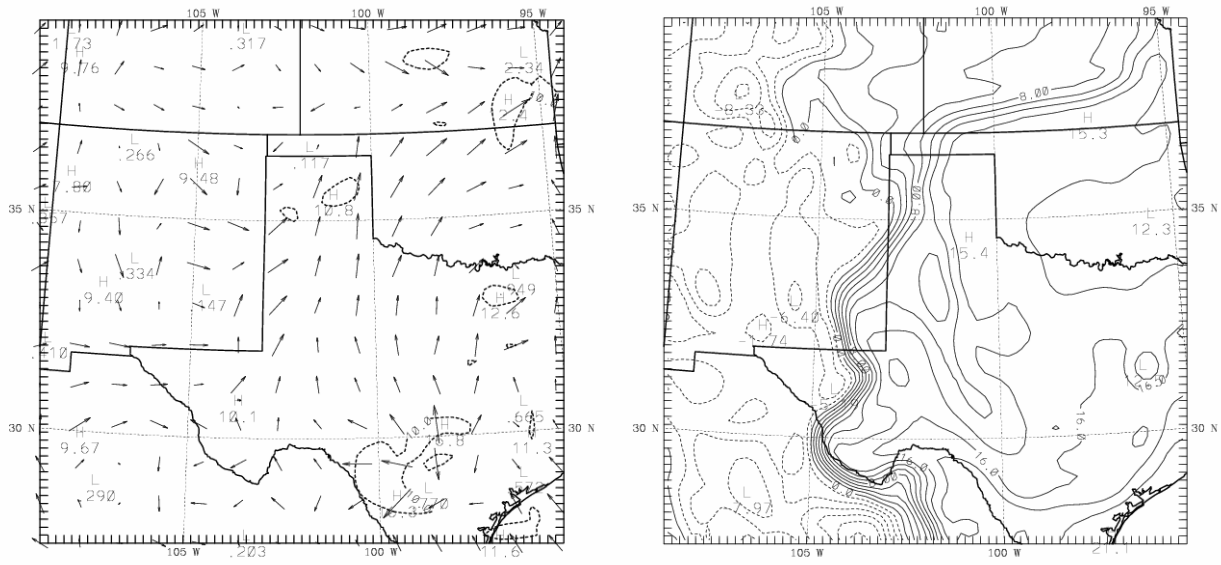
Fig. 7 36-h simulated surface vector winds (m/s) and $T_d$ ($^o$C) for E1



Fig. 8 Simulated 36-h accumulated precipitation (cm) for CNTR
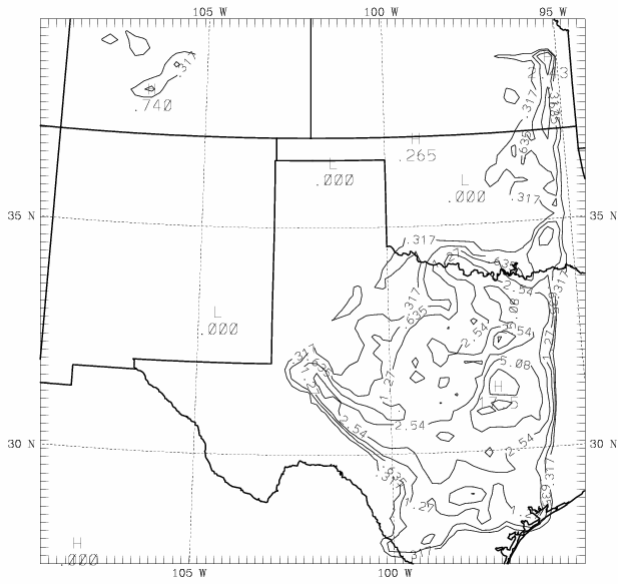
Fig 9 Simulated 36-h accumulated precipitation (cm) for E1



Precipitation data for the 24 hours ending 09-May-05, 13 UTC
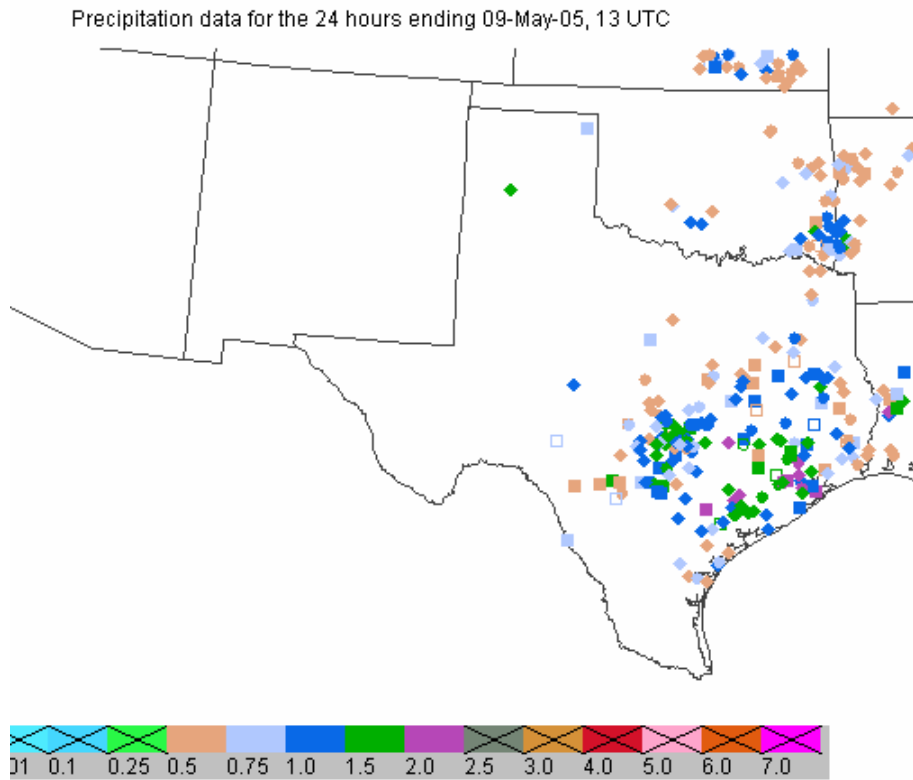
Fig. 10 Observed 24-h accumulated precipitation observed at 1200 UTC, 9 May 2005

Vector wind (m/s)

T ($^{o}$C)

q (gm/km)

(a) 24 h

14

Vector winds (m/s)  T ($^{o}$C)

q (gm/kg)

(b)

Fig 11 Simulated (CNTR-E1) surface vector wind, T, and q differences at (a) 24 h and (b) 36 h.

15
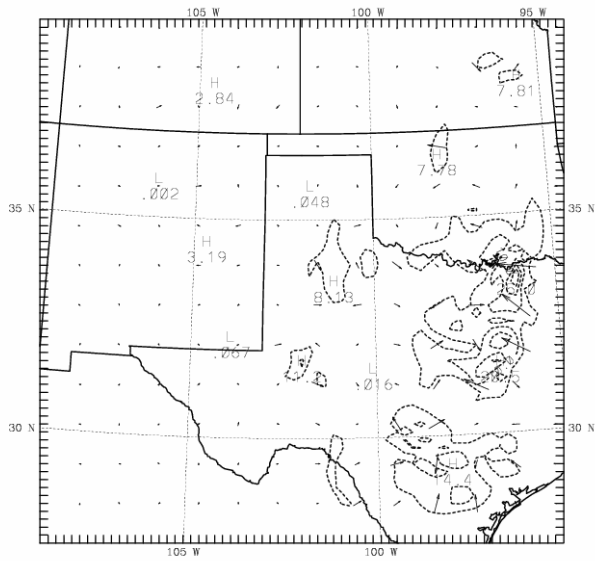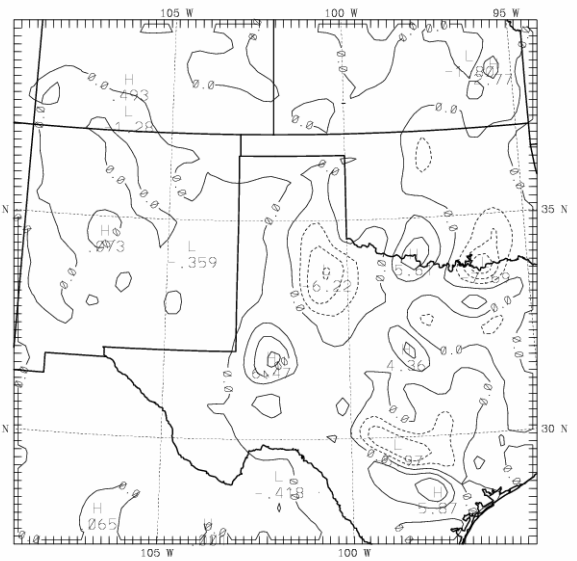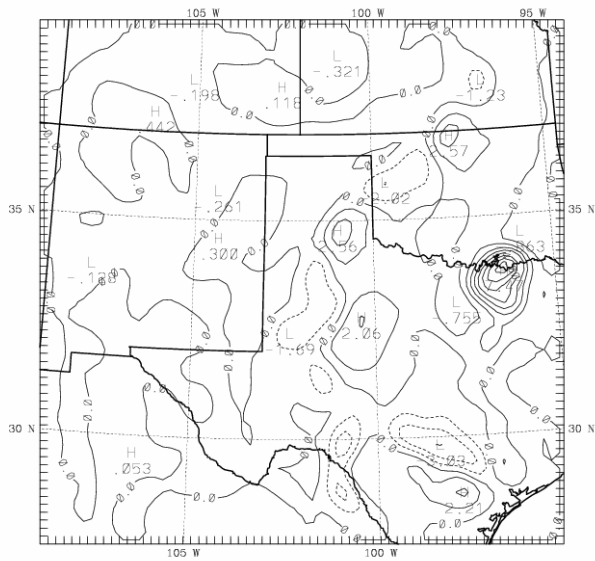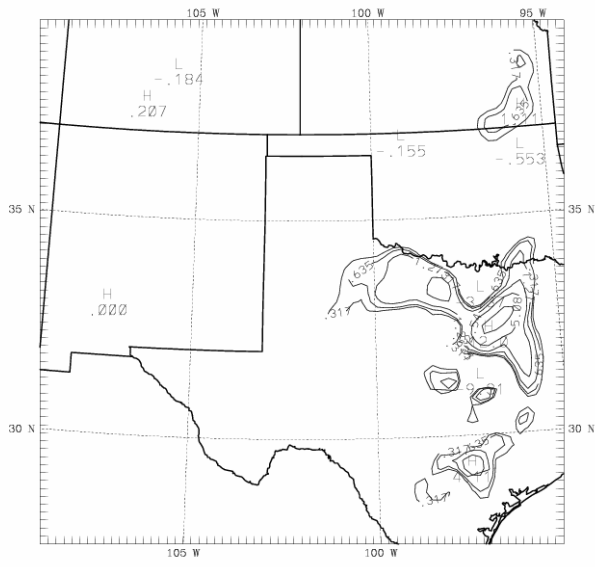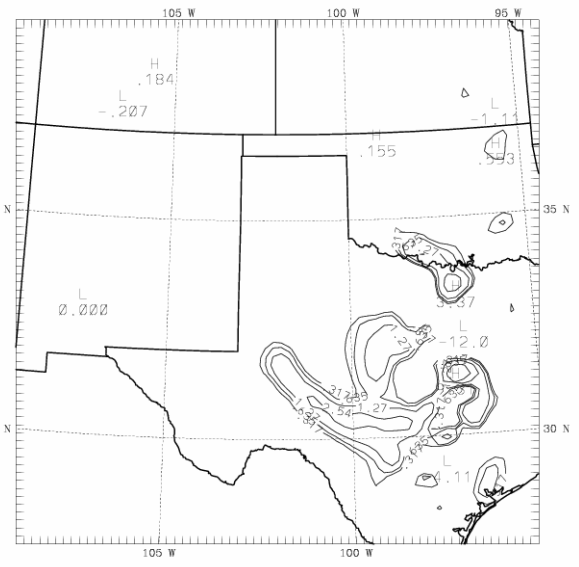
(a)   CNTR-E1                                    (b) E1-CNTR

Fig. 12 Simulated 36-h accumulated precipitation differences (cm)
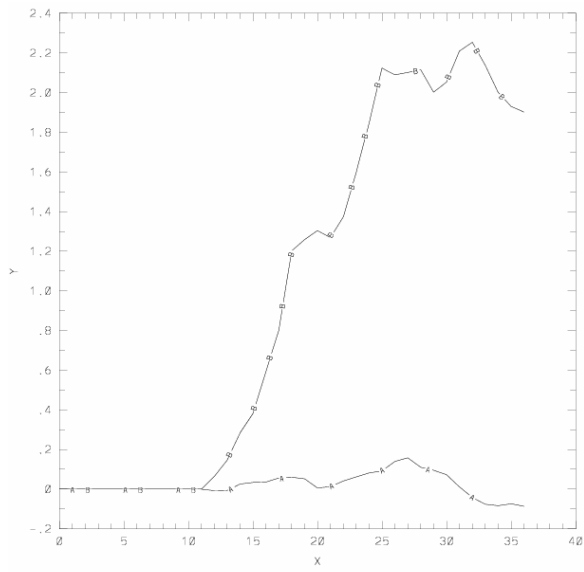
(a) u (m/s)                                       (b) v (m/s)
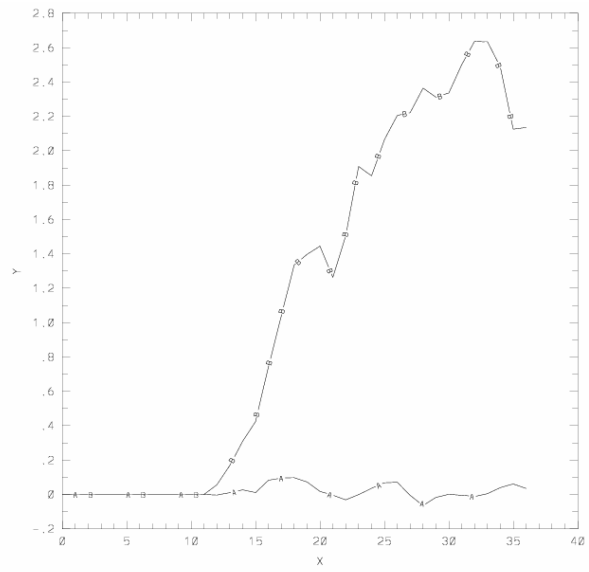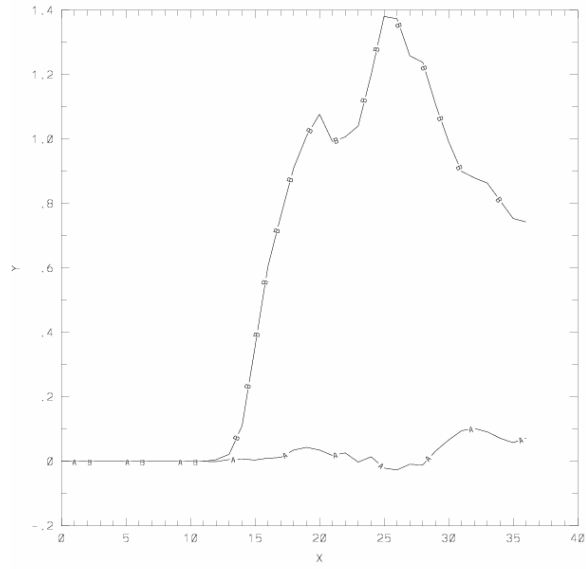
(c) T ($^{o}$C)

Fig. 13 Mean (Curves A) and standard deviation (Curves B) of (CNTR-E1) at the surface as a function of time (h) for (a) u, (b) v, and (c) T.
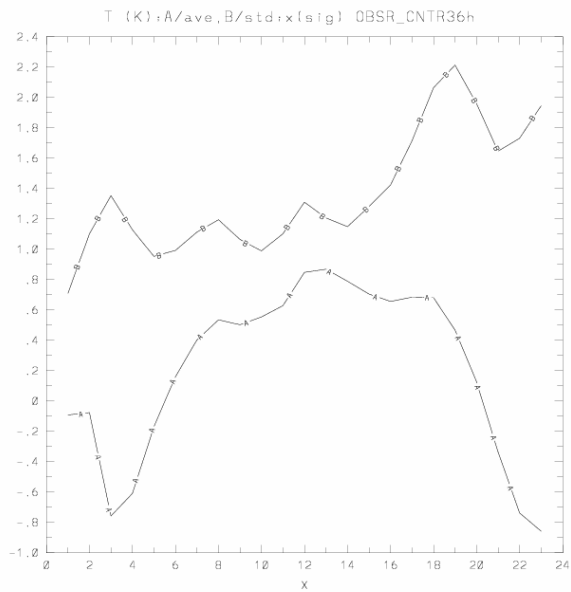


(a)  u (m/s)



(b) v (m/s)

17
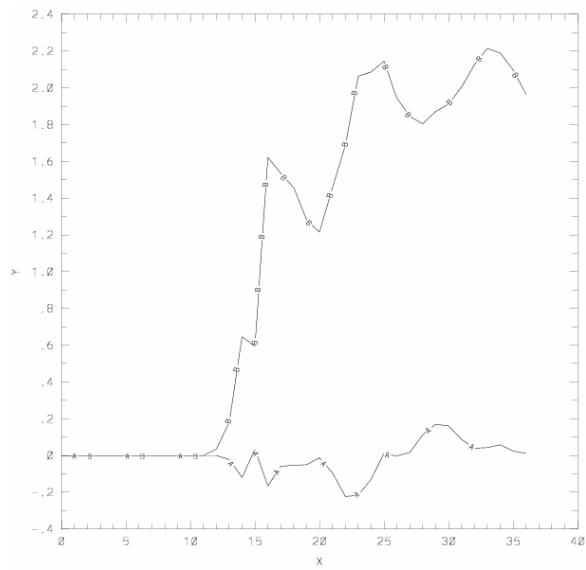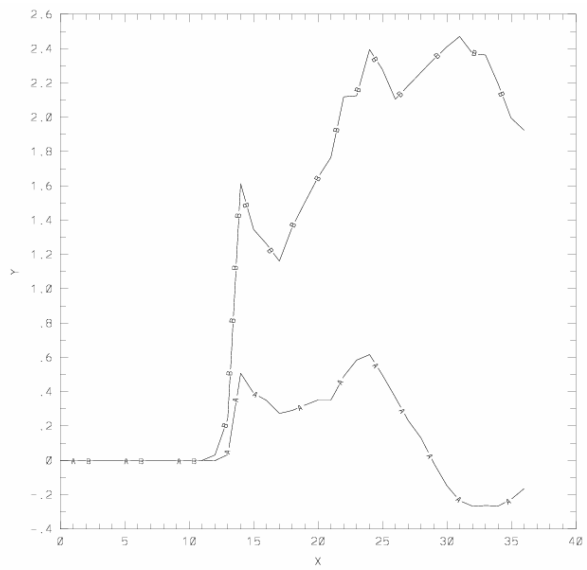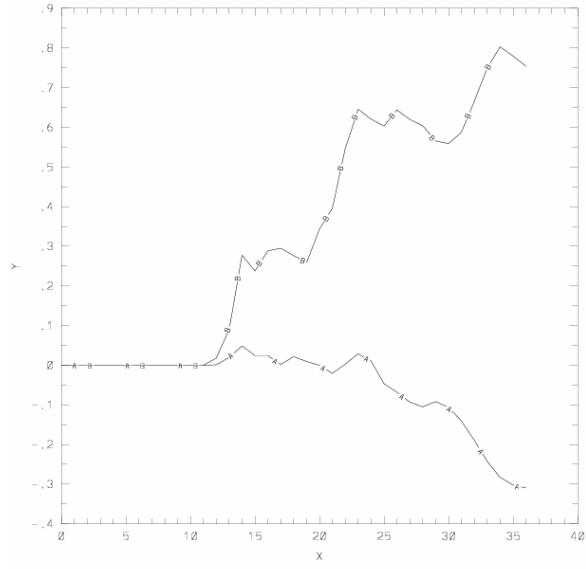
(c) T ($^o$C)

Fig. 14 As in Fig. 13 but at σ = 0.525 (~500 hPa).
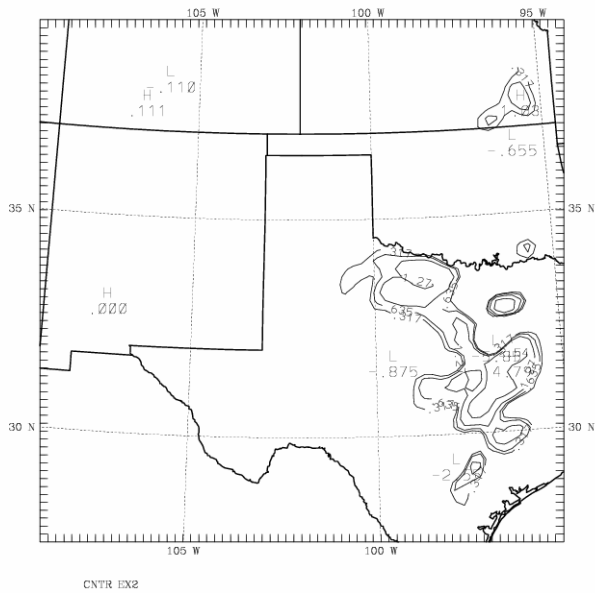
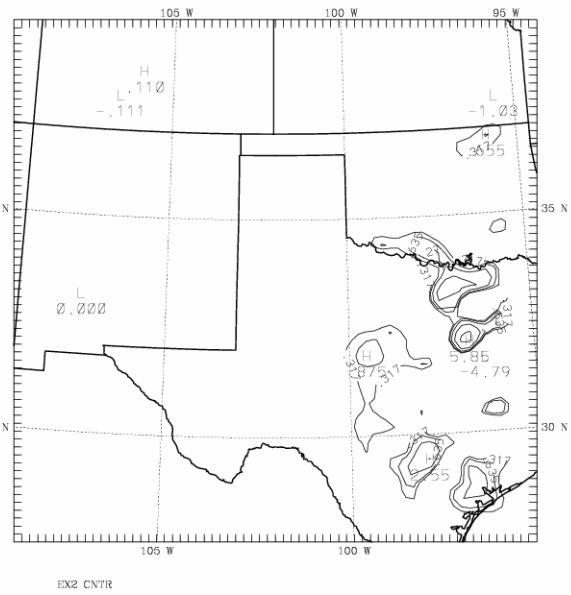

(a) u (m/s)



(b) v (m/s)

18
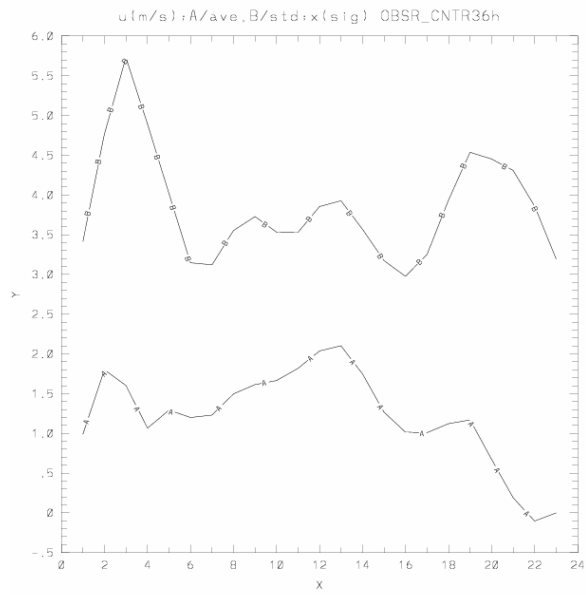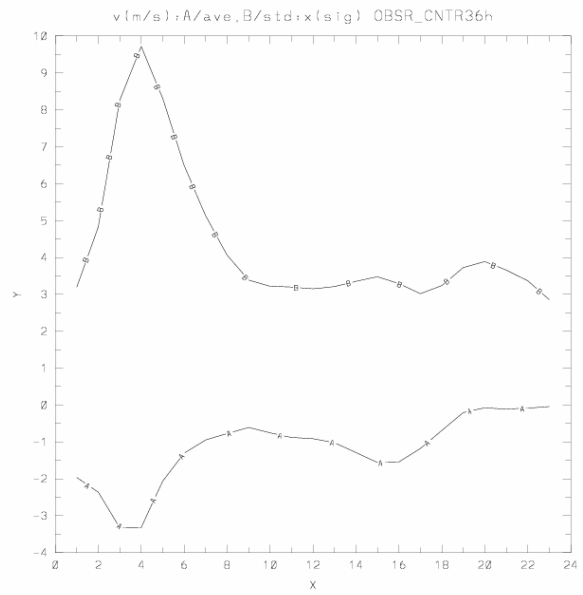
(c)  T ($^o$C)

Fig. 15 Mean (Curves A) and standard deviation (Curves B) of (Observation-CNTR) difference fields at 36 h as a function of model levels.
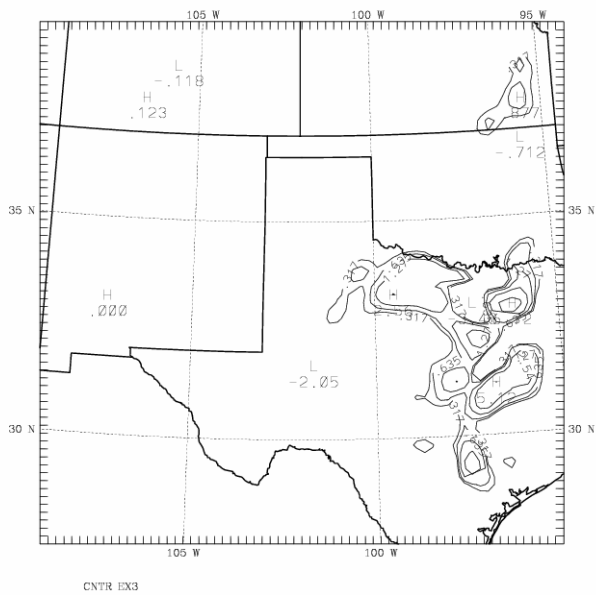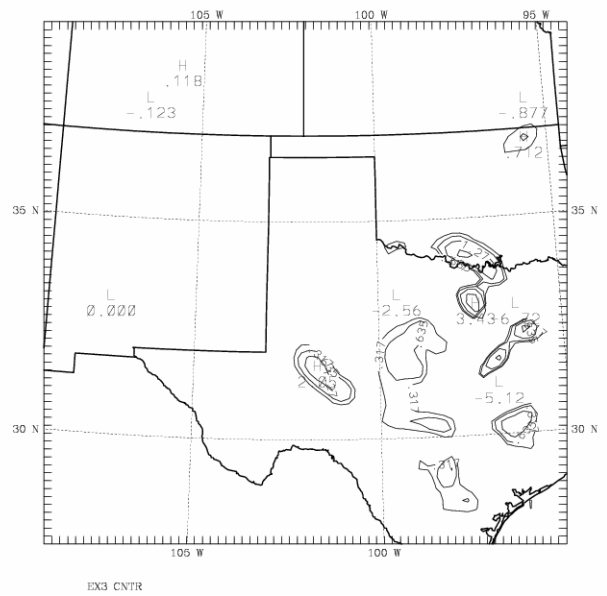


CNTR-E2                                                E2-CNTR

(a)

CNTR-E3                                    E3-CNTR

(b)

Fig. 16 Simulated 36-h accumulated precipitation differences (cm) for (a) CNTR-E2 and E2-CNTR and (b) CNTR-E3 and E3-CNTR